Chapter 4

Site subtitution driven antisite disorder in La_2NiMnO_6

4.1 Introduction

The B(B$^{'}$) cationic ordering influences the functional properties of double perovskites [12, 26, 31, 61, 138–140]. Moreover, the magnetic properties of $A_2BB^{'}O_6$ systems strongly rely on the valence states of cations and oxygen octahedra arrangements. Physical properties like spin glass, exchange bias, and spin dynamics in such compounds strongly depend on Ni^{2+}-O^{2-}-Mn^{4+} exchange interactions that determine the spin ground state [12, 26, 61]. The doping in double perovskites influences the local structure (bond length and bond angle) and disorder. The antisites disorder (ASD) in these compounds resulting from distortion in a corner shared MnO_6(NiO_6) octahedra that further originates the antiphase boundary (APB) [12, 26, 61]. The degree of ASD and APB governs multiple magnetic properties such as magnetization relaxation dynamics in the spin-glass phase and exchange bias mechanism [12, 26, 61].

Different approaches like doping, synthesis route, and processing conditions have been utilized to control the degree of antisites disorder [36, 50, 141–143]. Previous investigations indicate that the elemental variation of A-sites also plays a significant role in deciding the characteristics of the double perovskites [36, 50, 141–145]. A-site substitution also modifies (Ni/Mn)-O bond-length and Ni-O-Mn bond-angle [144–147]. Substituting A-site with another likewise element A$^{'}$ induces spin rearrangements [36, 50, 141–143]. For example, Sahoo *et al.* have reported that antisites could produce exchange bias and memory effect for the case of $LaSrCoFeO_6$ [141]. Guo *et al.* have found a tunable exchange bias field in polycrystalline $La_{2-x}Sr_xMnNiO_6$ [143]. A variable valence and spin

state have reported in ferromagnetic $La_{2-x}Sr_xMnNiO_6$ (x = 0, 0.1, 0.2) [142]. The A-site substitution influences the octahedral distortion, cation ordering, and degree of antisites disorder in the system lattice [148, 149].

Utilizing the above conceptualizations, the present study explores the polycrystalline compound $La_{2-x}Sm_xNiMnO_6$ where Sm-substitution is used to create a monotonic variation of the average cationic radii driven from the notable difference in ionic radii of La^{3+} and Sm^{3+}. This modification is predicted to influence the structural, electronic, and magnetic properties profoundly. The influence of partial substitution of La through Sm on the structural, magnetization, spin-glass, and memory characteristics of the $La_{2-x}Sm_xNiMnO_6$ still remains elusive. As discribed before, the samples were synthesized using *sol-gel* synthesis routes. The samples named S_0, S_1, and S_2 with different constituents of Sm in $La_{2-x}Sm_xNiMnO_6$ (x = 0, 0.1, 0.2). By utilizing XRD and Raman spectroscopy to explore the variation of the degree of antisites disorder as a function of Sm composition. This report also emphasizes describing the effect of Sm substitution on the exchange bias effect, spin-glass transition, relaxation dynamics, and magnetic memory effect. Magnetization decay and rejuvenation of the spin-glass phase of $La_{2-x}Sm_xNiMnO_6$ are also described.

4.2 Results and discussion

4.2.1 Structural and surface morphology

Figure (4.1(a, b & c)) depicts the XRD patterns of the S_0, S_1, and S_2. Rietveld's refinement of the XRD patterns suggests that observed peaks are well matched with a combined phase of monoclinic ($P2_1/n$) and rhombohedral (R3c) crystal structure for S_0 [150]. In contrast, analysis of (S_1 and S_2) suggests a single monoclinic ($P2_1/n$) phase.The most notable peaks are indexed for both phases (monoclinic+rombohedral) for sample S_0 using the subscript of the corresponding phase. Fig. (4.1(d & e)) shows the relative comparison of the brightest XRD peak for S_0, S_1, and S_2. The presence of a rhombohedral phase with monoclinic ($P2_1/n$) is evident for S_0 sample from peak splitting at $2\theta = 33^\circ$ [148], that converges with Sm for S_1, and S_2. The S_1, and S_2 samples show only a pure monoclinic ($P2_1/n$) structure. The peaks around 32, 40, and 59 degrees have a notable doublet characteristic for sample S_0, while the same peak for S_1 and S_2 shows a singlet peak. The enlarged view of peaks around 32 and 59 are indexed with rhombohedral and monoclinic phases (see Fig. (4.1(d & e))). Fig. (4.1(d & e)) confirms that sample S_0 have biphasic. The goodness of fit (GOF) for samples S_0, S_1, and S_2 are 1.8, 1.6, and 1.7, respectively and other fitted parameters are mentioned in Table (4.1).

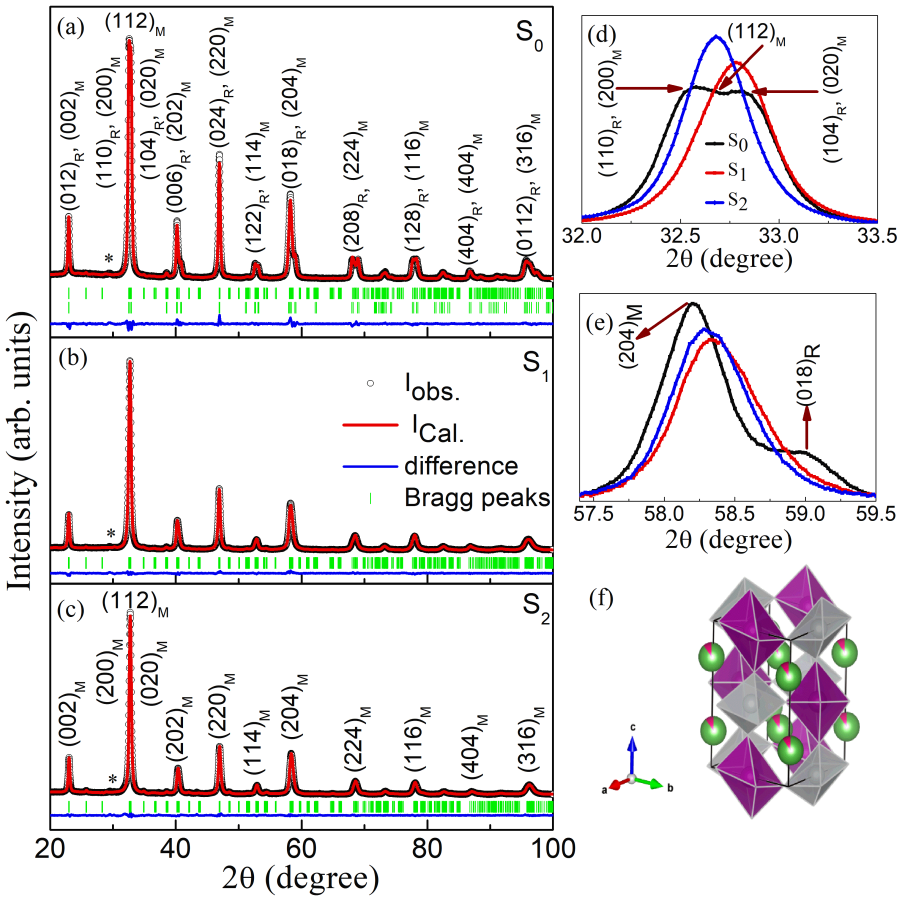

Fig. 4.1 (a) The XRD patterns of S_0, (b) S_1, and (c) S_2 along with Rietveld refinement where black circle, red-line, blue-line, and green spike represent the experimental data, refined fit, their difference, and indexed Bragg's peaks, respectively. (d & e) shows the relative comparison of $La_{2-x}Sm_xNiMnO_6$ (where x = 0, 0.1, 0.2) and peaks belonging to the rhombohedral phase for sample S_0. (f) the local crystal structure of $La_{1.8}Sm_{0.2}NiMnO_6$ where NiO_6 and MnO_6 octahedra indicated by grey and purple colour, respectively. The symbol * across 30° indicates the presence of negligible secondary phases present in all samples.

The Sm^{3+}($r_{Sm^{3+}}$ = 1.132 Å) replacing the La^{3+} ($r_{La^{3+}}$ = 1.216 Å) has smaller radii that change the bond-length (Ni/Mn-O) and bond-angle (Ni-O-Mn). To estimate the influence of Sm-substitution on the structural characteristics, we use the Shannon table [151] to select the values of the ionic radius for the elements of A-site and the tolerance factor. The effective radius r_A of upon A-site substitution is defined by: $r_A=(2-x).r_{La^{3+}} + x.r_{Sm^{3+}}$. The r_A values (see Table (4.1)) are estimated considering elements occupying site-A atoms that have coordination number 9. The coordination number of site-A atoms for the perovskite compound is 12. Still, in the presence of profound distortion of MnO_6 octahedral, the effective coordination number of the total polyhedron of the A-site atoms is reduced to 9.

Table 4.1 Structural parameters obtained from Rietveld refinement for S_0, S_1, and S_2 samples.

Sample	S_0		S_1	S_2
	$P2_1/n$ (44%)	R3c (56%)	$P2_1/n$	$P2_1/n$
a (Å)	5.5099	5.5096	5.5068	5.4912
b (Å)	5.4502	5.5096	5.4594	5.4533
c (Å)	7.7433	13.2623	7.7384	7.7436
β (°)	90.03	-	90.13	89.83
V (Å^3)	232.53	348.65	232.65	231.88
r_A (Å)	2.432		2.424	2.415
Tolerance factor	0.920		0.919	0.917
Ni-O_1 (Å)	1.0391		1.5165	1.9381
Ni-O_2 (Å)	1.9219	1.9122	1.9398	2.0158
Ni-O_3 (Å)	1.9549		2.0008	1.6118
Mn-O_1 (Å)	2.8429		2.3795	2.1138
Mn-O_2 (Å)	1.9781	1.9792	1.9866	1.8557
Mn-O_3 (Å)	2.0278		1.9046	2.2917
∠Ni-O_1-Mn (°)	171.62		168.4528	145.45
∠Ni-O_2-Mn (°)	166.81	168.11	161.8410	176.27
∠Ni-O_3-Mn (°)	153.03		164.3804	165.16
R_p	5.86		5.34	5.70
R_{wp}	5.60		5.15	5.62
R_e	3.04		3.26	3.24
χ^2	3.3		2.4	3.0
ρ (g/cc)	6.962	6.965	6.975	7.014

The lattice parameters, bond-length & bond -angles derived from Rietveld refinements are mentioned in Table (4.1). The octahedra of NiO_6 expand in the planer direction, and MnO_6 compress in the planer direction, suggesting octahedra tilting with Sm-concentration. The sample S_0 has a higher Mn-O bond length due to the rhombohedral phase with higher symmetry and distortion that transforms into a lower distorted monoclinic phase. The Rietveld refinement explains the avg. bond-length of <Ni-O> increases and <Mn-O> decreases with Sm concentrations. The average bond angle (Ni-O-Mn) decreases with increasing Sm-concentration, suggesting that the octahedra tilting increases, further affecting the ordering temperature. The Sm-substitution decreases the unit cell volume, resulting in modified lattice parameters a, b, and c, average bond-angle Mn(Ni)–O–Ni(Mn) and the average distance Mn(Ni)–O [152]. The modified volume permits the effects at A-site to be more pronounced. Such modification can be understood as the size effect of the A-site. The average bond length (Ni/Mn-O) increases when Ni/Mn bands overlap due to unit cell compaction. $La_{1.8}Sm_{0.2}NiMnO_6$ compound favours higher distorted unit cell due

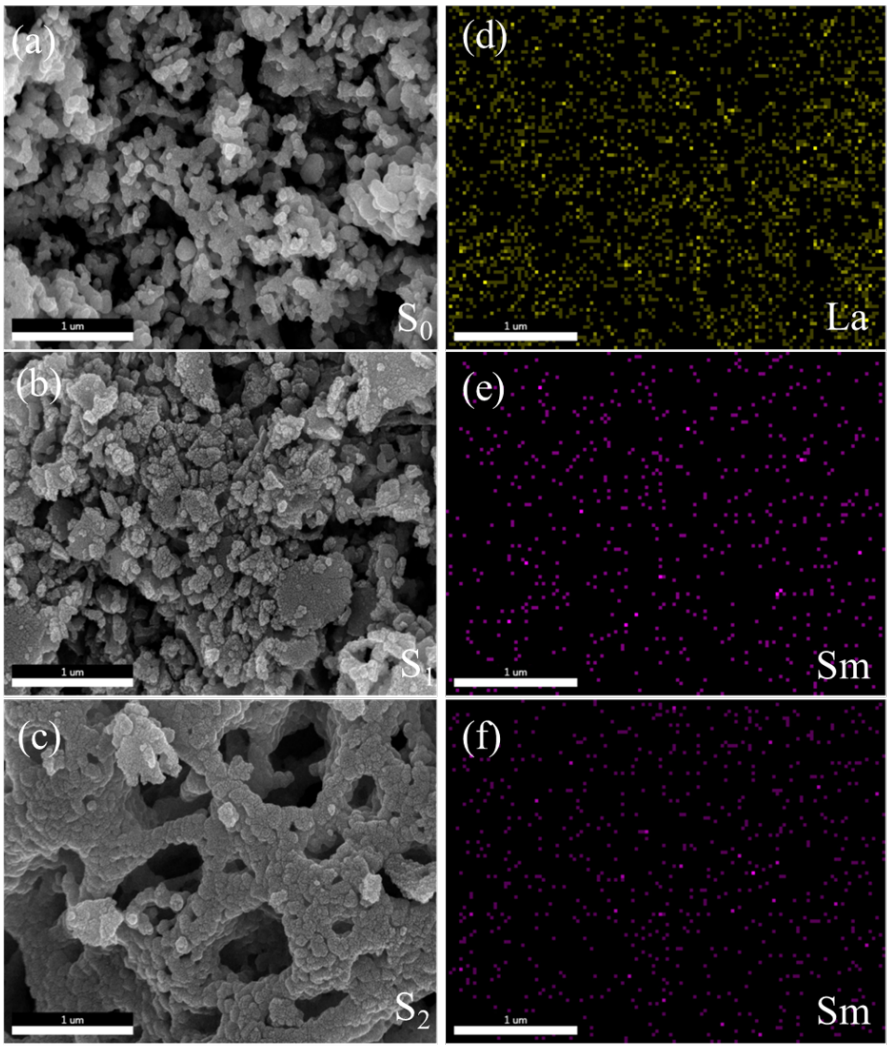

Fig. 4.2 (a, b, & c) FESEM micrograph of S_0, S_1 and S_2, respectively. (d, e, & f) distribution of La and Sm in S_0, S_1 and S_2, respectively.

to a lowering in tolerance factor, resulting in a reduced symmetry structure (monoclinic), that well corroborates with our experimental observations (see Fig. (4.1)). The local crystal structure of $La_{1.8}Sm_{0.2}NiMnO_6$ depicted in the inset of Fig. (4.1(b)) that demonstrates the bonds are stretched and compacted in some direction indicates distortion.

To determine the particle size and geometry and their cation spatial distribution, FESEM imaging of $La_{2-x}Sm_xNiMnO_6$ (where $x = 0, 0.1, 0.2$) is conducted. Figure (4.2(a, b & c)) shows the FESEM images for S_0, S_1 and S_2 that confirm the particle agglomeration at the nanoscale. The prominent characteristics of these nanostructured materials depend on their size, shape, and spatial distribution. The cation distributions shown in Fig. (4.2(d, e & f)) indicate the homogeneous distribution of La and Sm cations through elemental mapping

and FESEM. The elemental mapping in sample S_0 indicates that various crystallites rather than the cations form the agglomeration, and its distribution is nearly homogeneous. The Sm-concentration increases from S_1 to S_2 also confirmed by the mapping and its distribution is also uniform, as clearly visible in Fig. (4.2(e & f)). Table (4.2) represents the chemical composition of samples (S_0, S_1 and S_2) by quantitative analysis through energy Energy-dispersive X-ray spectroscopy (EDX) measurement. The EDX spectra show the composition corresponding to samples in nominal fraction within standard deviations.

Table 4.2 Quantification of Samples S_0, S_1 and S_2 by EDX after excluding oxygen.

Element	Sample (S_0)		Sample (S_1)		Sample (S_2)	
	Expected (%)	Observed (%)	Expected (%)	Observed (%)	Expected (%)	Observed (%)
La	57	57.26	54.02	56.1	51.05	53.8
Sm	-	-	3.08	3.38	6.14	6.57
Ni	12.04	13.47	12.01	13.35	11.98	13.2
Mn	11.27	11.57	11.25	11.29	11.22	12.0

The TEM images utilized to determine the particle size and the geometry of samples are shown in Figure (4.3(a)). The geometry of agglomerated particles was recognized as distorted rhombohedral and hexagonal. The TEM images indicate the quantitative average particle size is 10-50 nm. The particles are agglomerated and merged. Fig. (4.3(b)) enlarged view of selected nanoparticles that further hints at the geometry and size. The HR-TEM images correspond to selected regions confirmed through lattice imaging. The reported interplanar spacing between these planes is 0.3871 nm, which is well-matched with the lattice plane (002).

4.2.2 Magnetic characterstics

Figure (4.4(a)) shows M-T recorded in the ZFC/FC protocols for all samples under an externally applied magnetic field 100 Oe. The sample S_0 shows paramagnetic $\rightarrow$ ferromagnetic transition across T_c (284 K) due to superexchange interaction between Ni^{2+}-O^{2-}-Mn^{4+} cations as reported previously [25, 26, 53, 62, 68, 95]. Multiple spin ordering transitions are seen in the M-T at a lower temperature, and the most pronounced T_{SG} across 50 K presents the spin-glass phase transformation from a ferromagnetic state. T_c is extracted by the derivative of M-T as shown in the inset of Fig. (4.4(a)). Across T_c, observed bifurcation between the M-T acquired in ZFC/FC protocol indicates the presence of frustrated magnetic states such as spin-glass, cluster glass, and superparamagnetic (SPM) states. Other prominent features that can be noticed in the M-T are as follows (i) reduced T_c, (ii) enhanced M_s values, and (iii) low-temperature magnetization anomalies. The magnetic

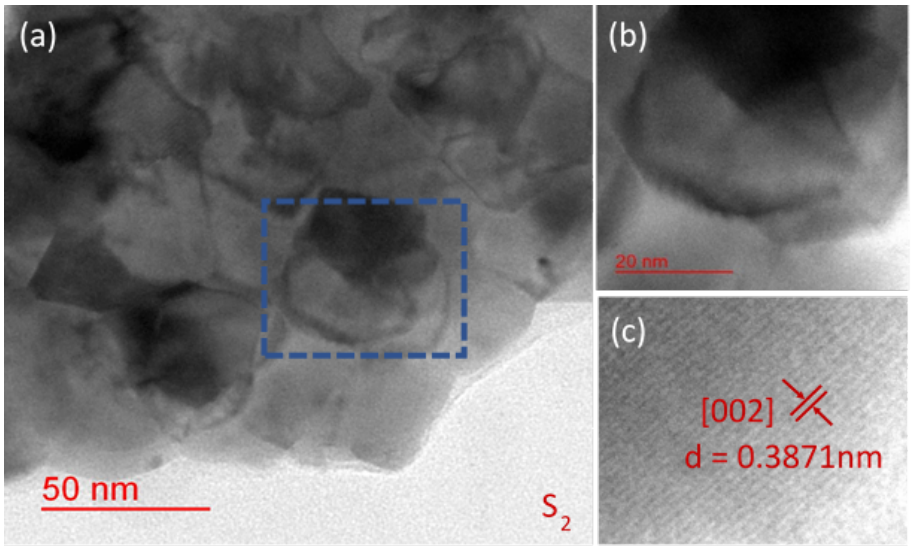

Fig. 4.3 (a) TEM micrograph of S_2, (b) High-resolution images(HRTEM) micrograph of marked area (c) lattice images of a selected area.

properties of the $La_{2-x}Sm_xNiMnO_6$ compounds show a ferromagnetic transition at the T_c that decreases with the Sm-substitution. The observed T_c are 284, 253, and 245 K for samples S_0, S_1, and S_2, respectively.

The T_c of $La_{2-x}Sm_xNiMnO_6$ compound decreases with Sm-proportion because of reduced ionic radii and resulting unit cell distortion. The T_c that depends on the Mn(Ni)-O-Ni(Mn) bond-angle and Ni/Mn-O bond-length upon Sm-substitution unit cell distortion, tolerance factor, and cation ordering can modify. Modified unit cell parameter influences the bond-length and bond-angle. The T_c is decreased with Sm-doping due to lowering the Ni(Mn)-O-Mn(Ni) bond angle. Magnetic anomalies at lower temperatures emerge due to the *3d-4f* interaction that helps to stablize the spin-glass phase.

Figure (4.4(b)) shows the isotherm M-H recorded at 5 K in the $\pm$ 15 kOe range in FC condition from 300 K with continuous applied magnetic field +500 Oe. The M_s value increases with Sm-content suggesting that the Sm improves B-site cation ordering. The coercive field H_c, remanence magnetization M_r, and other magnetic parameters of samples S_0, S_1, and S_2 as a function of Sm-concentration are listed in Table (4.3).

Table 4.3 Magnetic parameters of $La_{2-x}Sm_xNiMnO_6$ where (x = 0, 0.1, 0.2).

Sample	T_c (K)	M_s (emu/g)	H_c (Oe)	M_r (emu/g)	H_{EB} (Oe)
La_2NiMnO_6 (S_0)	284	24.1	650	3.64	120
$La_{1.9}Sm_{0.1}NiMnO_6$ (S_1)	253	28.7	762	11.50	39
$La_{1.8}Sm_{0.2}NiMnO_6$ (S_2)	245	34.0	580	10.33	28

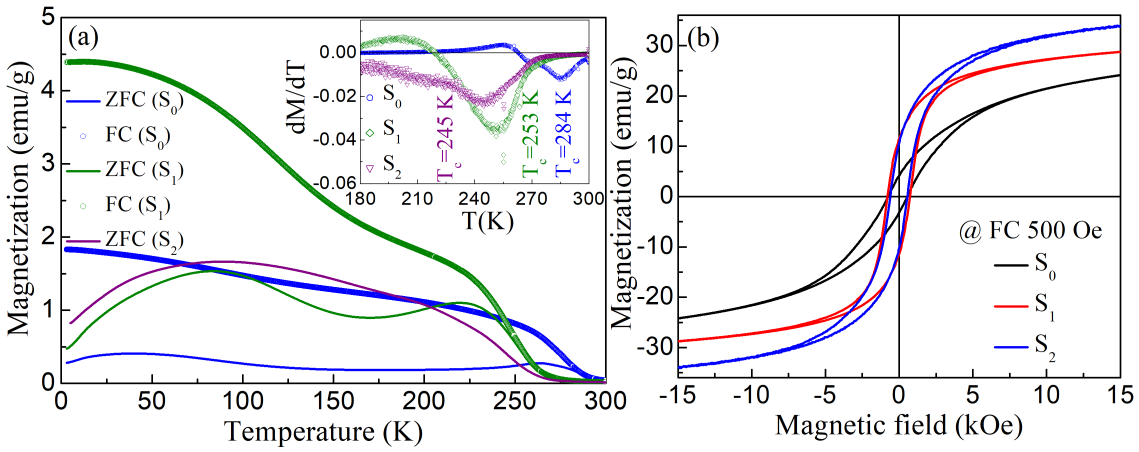

Fig. 4.4 (a) dc-magnetization variation with temperature in ZFC/FC mode with 100 Oe magnetic field for samples S_0, S_1, and S_2. Inset is the plot for the dM/dT, (b) Isothermal magnetization measurement at 5 K under an applied magnetic field of +500 Oe for S_0, S_1, and S_2.

The magnetic moment of Sm, the Ni(Mn) cationic ordering, and the magnetic interaction between (Sm-Ni/Mn) all contribute to the values M_s. To understand the impact of doping on antiphase boundaries in the magnetic frustrated state at a lower temperature, we recorded the M-H loops in the FC protocol to measure the exchange bias. To avoid any minor loop effects, the M-H loop was measured at $\pm$ 15 kOe. Figure (4.5(a, b, and c)) depicts the M-H loops in the range of $\pm$ 2 kOe for samples S_0, S_1, and S_2, respectively. The samples field cooled from 300 to 5 K under an external magnetic field of +500 Oe, and the M-H loops were recorded (blue line) Fig. (4.5). The M-H loops indicate a pronounced shift in the opposite direction for the FC procedure with opposite field polarity, *i.e.*, -500 Oe (red line), that indicate the presence of exchange bias in $La_{2-x}Sm_xNiMnO_6$ [48, 51, 52, 153, 154]. Fig.(4.5(a)) portrays the M-H) loop acquired in ZFC protocols with no exchange bias. In FC conditions, the exchange is detected in all samples S_0, S_1, and S_2. The M-H loops are found to be shifted in the presence of various field-cooled conditions, confirming the exchange bias. At Sm-concentration increases, the exchange bias magnitude is reduced (Fig. 4.5). The exchange bias field for samples S_0, S_1, and S_2 are found to be 120 Oe, 39 Oe, and 28 Oe, respectively. These results indicate that the strength of the exchange bias field reduces as antisites disorder decreases. A similar study using $La_{1.5}Ca_{0.5}CoMnO_6$ double perovskite has also reported the role of antisite-disorder on induced exchange bias effect [155]. Exchange bias also manifests in other site substituted double perovskite systems [50, 156, 157].

The measurement real part of ac-susceptibility χ' as a function of frequency (ω) and temperature were recorded to explore various signatures of the magnetic frustrated state

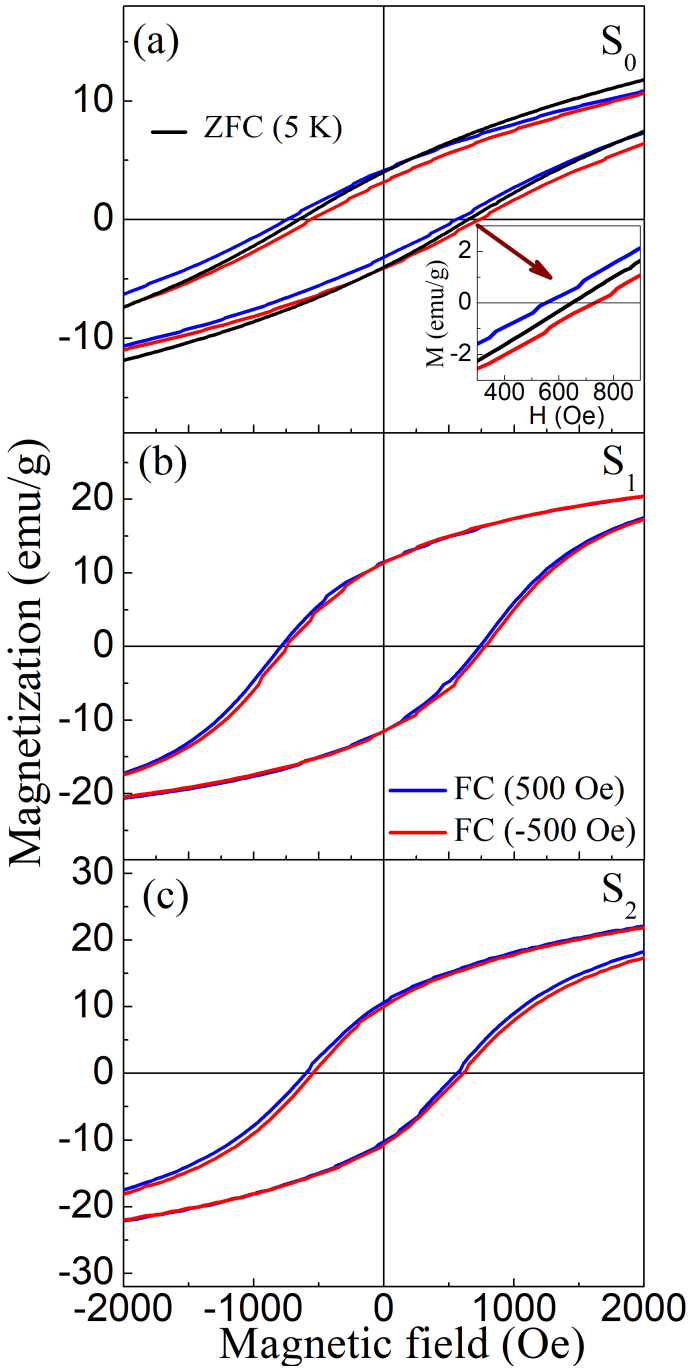

Fig. 4.5 Magnetization loops collected at 5 K. Before measurements the sample was field cooled from 300 K in the presence of the applied magnetic field of ± 500 Oe (blue, red lines), suggesting the evolution of exchange bias for S_0, S_1, and S_2 in panel a, b, and c, respectively. Black line in panel a represent for M-H loop in ZFC. Inset shows an enlarged view of the panel (a).

that dominate at lower temperatures. The variation in $\chi^{'}(\omega,T)$ for S_0 and S_2 is shown in Figure (4.6(a & b)). As a function of ω, the reported cusp is shifted toward the higher

temperatures side. The shift of cusp location with ω for S_0 and S_2, confirms the existence of the spin-glass (SG) or cluster glass (CG) states. For S_2, Sm doping shifts the T_{SG} towards the higher temperature as Sm-content increases. A frequency-driven shift in T_{SG} is a typical signature of the spin-glass state. To examine the origin of spin relaxation and its dynamics, the Mydosh parameter expresses as (Ω)= ($1/T_f(\omega)$)*($\Delta T_f(\omega)/(\Delta \ln(\omega))$ is calculated [39, 131]. $\Delta T_f(\omega)$ is the peak shift as a function ω. In the case of magnetic frustration originating the cluster glass freezing, Ω spans across 0.005–0.090. While Ω ranges from 0.1–0.3 for the SPM phases. In this case, the estimated Mydosh parameter Ω of 0.004 and 0.005 for samples S_0 and S_2 indicates that frequency dispersion is mainly driven by cluster or spin-glass freezing [39, 131]. Therefore, the presence of any SPM state in these compounds can be ruled out.

Herein, the dynamics characteristics of the spin-glass phase that emerges at lower temperatures below the spin-glass transition T_{SG} are investigated. The characteristic relaxation time τ using power law is analysed to understand the role of antisites in such complicated systems such as $La_{2-x}Sm_xNiMnO_6$. The average relaxation time τ_{avg} is temperature dependent, therefore, the characteristics of $\tau_{avg}(T)$ are used to explore the nature of magnetic frustration. The relaxation time τ associated with the temperature $T_f(\omega)$. The τ is determined using the expression $\tau = 1/\omega$. Power-law that predicts critical slowing down spin dynamics shows its divergence at T_{SG} is always utilised to understand the frequency dependence of the spin-glass freezing temperature $T_f(\omega)$. The divergence at T_{SG} can be modelled through $\tau = \tau_0 \left(\frac{T_f(\omega)-T_{SG}}{T_{SG}}\right)^{-z\nu}$ where T_{SG} is the spin-glass transition temperature, τ_0 is the inverse of the frequency. The critical exponent of the correlation length express as $\xi = \left(\frac{T_f}{T_{SG}} - 1\right)^{-\nu}$ and z is the dynamic exponent that given as $\tau \sim \xi^z$ [39, 131].

Fig. (4.6(c & d)) shows the least-square fit of the τ versus T_f plot shown as a solid line. The resulting fit parameters are as follow, T_{SG} = 45.5 K, $\tau_0 = 8.6 \times 10^{-11}$ s, and $z\nu$ = 8.96 for sample S_0. For sample S_2, the fitted parameters are T_{SG} = 72.9 K, τ_0 = 6.7 $\times 10^{-10}$ s, and $z\nu$ = 7.23. For conventional spin glasses, τ_0 usually spans over $\sim 10^{-10}$ –10^{-13} s and $z\nu$ varies between $\sim$ 4-13 [158]. It is essential to note that the value of τ_0 ranges across $\sim 10^{-10}$ -10^{-13} s that changes the T_{SG} and T_f that are greater than $\pm$ 10 K. Larger value of τ_0 indicates slow dynamics for randomly spin cluster glasses which fundamentally differs from atomic level randomness as in the case of a traditional spin-glass. Similar τ_0 values have been observed in other likewise systems such as magnetites and perovskite nanoparticles [12]. Fig. (4.6(c & d)) shows the observed nonlinearity that rules out the SPM phase that evolves due to blocking for the reported cusp as seen in ZFC dc-magnetization and ac-susceptibilities across T_{SG}.

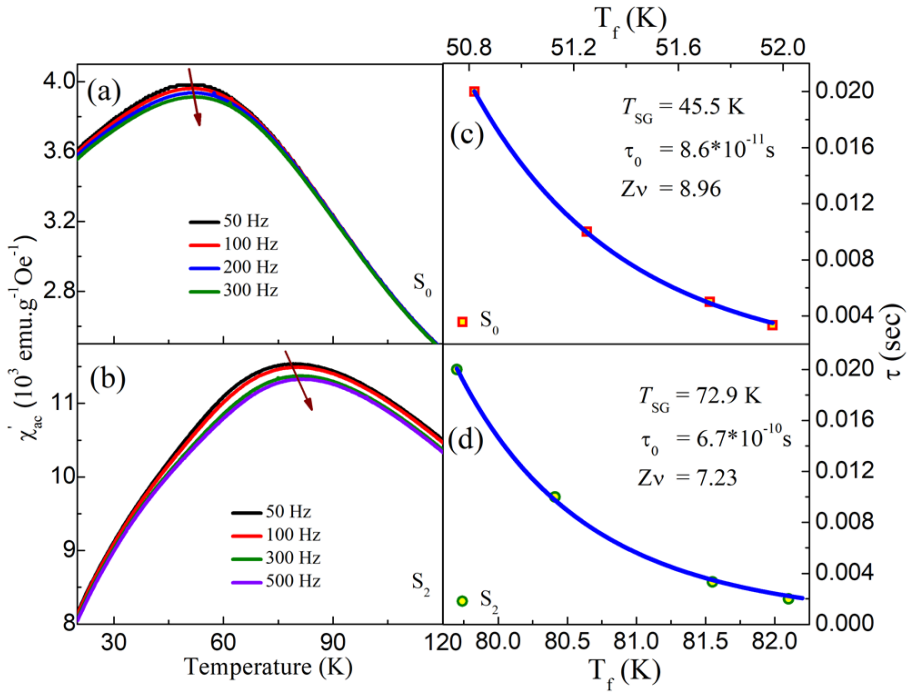

Fig. 4.6 Real part of ac- susceptibility ($\chi^{'}$) as a function of temperature for (a) S_0, and (b) S_2 reported at various frequencies. Power law fitting of relaxation time (τ) as a function of temperature for samples (c) S_0, (d) S_2.

The stretched exponential characteristics are predicted in strongly interacting systems such as spin-glasses and spin clusters [159, 160]. Thermoremanent magnetization (TRM) can be expressed as $M(t) = M_0 + M_r \exp[-(t/\tau)^{1-n}]$, where M_r is a glassy component, M_0 presents the dc-magnetization, τ depicts the relaxation time, and n is stretched exponent [159, 160]. For a conventional SG system, n ranges across 0 and 1 [10, 39, 131, 161]. $n = 0$ indicates that the system behaves as mono-dispersive Debye-like relaxation, whereas $n = 1$ indicates the absence of any relaxation. For a frozen state of spin-glass system with a high number of degenerate states the values of n in the range $0 < n < 1$. Here, we found a slow relaxation of TRM in the glassy phase of samples S_0 and S_1. Prior to measurements of TRM, samples were first cooled from 300 to 10 K in the presence of an external magnetic field of +10 kOe; the magnetic field was then switched off, and magnetization decay as a function of time was measured. Figure (4.7) depicts the TRM relaxation curves (dotted symbol), with the fit (solid lines) of the stretched exponential function. The fitted parameters are $M_0 = 3.76$ emu/g, $M_r = 0.156$ emu/g, $\tau = (965 \pm 7)$ s, and $n = 0.644$ for sample S_0. The obtained parameter for S_1 are as follows: $M_0 = 9.52$ emu/g, $M_r = 0.498$ emu/g, $\tau = (1234 \pm 12)$ s, and $n = 0.622$. The fitted exponent values are

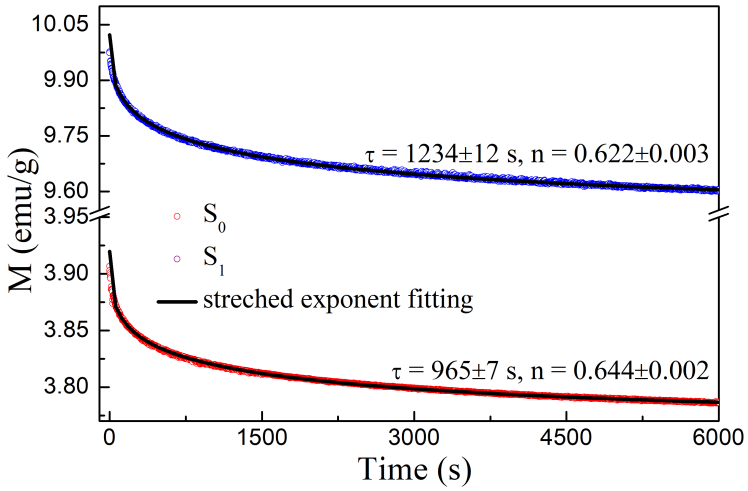

Fig. 4.7 Thermoremanent magnetization (TRM) relaxation data recorded at 10 K for S_0 and S_1. Before measurements, the samples were first field cooled from 300 K to 10 K under an applied magnetic field + 10 kOe.

well within the range of SG/CG [10, 161, 162], ruling out any possibility of the existence of SPM phase in these compounds.

4.2.3 Magnetic memory and rejuvenation

The heterogeneous spin configurations of the spin-glass phase display multiple exceptional properties like magnetic memory and rejuvenation properties [131, 163]. As proposed by the droplet model below T_{SG}, for such properties to exist a single spin state favourable in terms of free energy [164]. In contrast, hierarchical model [47] predicts a multi-valleyed spin configuration, which will be favoured that formed into new sub-valleys at reduced temperature. These sub-valleys will be merged at elevated temperatures. We employed multiple methods to examine these compounds' memory and rejuvenation effects.

To examine the memory effect, we applied a similar approach as proposed by Sun *et al.* [165]. First, we study the influence of a temperature cycle on the phenomena of magnetic relaxation. During ZFC, the sample was first cooled down in absence of any external magnetic field from room temperature down to 15 K with a sweeping rate of 15 K/min. Then the M(t) was recorded under an applied magnetic field 100 Oe from time (t) = 0 to final cycle time (t_1) = 3600 s (see Figure (4.8)). After the initial time cycle t = t_1, quenching was performed to 10 K, and the magnetization measurement was repeated at time t = t_2 = 3600 s, as depicted in Fig. (4.8). The sample temperature was steadily ramped

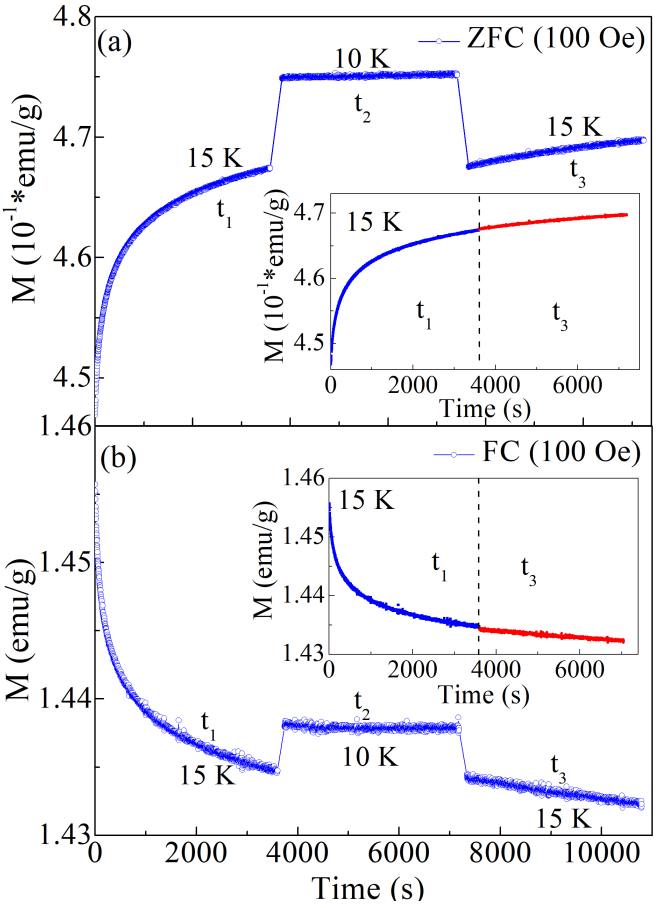

Fig. 4.8 Magnetic relaxation behaviour of sample S_0 recorded at 15 K with magnetic field 100 Oe for (a) ZFC and (b) FC protocols. The relaxation behaviour indicates that the characteristic curve for t_3 is an ongoing trend of the curve for cycle t_1 indicating a robust magnetic memory nature.

to 15 K and applied a magnetic field of 100 Oe. Then magnetization measurement at 15 K for time $t = t_3 = 3600$ s, as shown in Fig. (4.8). The M(t) curves recorded for duration time $t = t_3$ show the progress of the exact curve measured at time $t = t_1$, as depicted in the inset of Fig. 4.8. This method suggests that as the sample is recycled to 15 K, the starting temperature point is reattained.

During the FC procedure, the sample was cooled from room temperature to 15 K at a sweeping rate of 15 K/min in the presence of a magnetic field of 100 Oe. Then the magnetic field instantly reset to off, and M(t) data were collected for the duration $t = t_1 = 3600$ s. After completion duration for $t = t_1$, the sample was allowed to quench at 10 K (the field kept off) and the M(t) was monitored for time $t = t_2 = 3600$ s. At last, the sample was kept at 15 K, and M (t) was recorded throughout for duration $t = t_2 = 3600$ s. The initial state of the system is reattained then the temperature returns to 15 K, as depicted

in panel (b) of Fig. (4.8). Therefore, as clearly visible in the inset the relaxation of the magnetization M (t) curve at time t_3 represents the prolongation of $t = t_1$.

4.2.4 Raman Spectra

The degree of antisites disorder in double perovskites can be explored through Raman spectroscopy [36, 94, 166], which is a well-proven tool for determining the spin-phonon coupling, lattice distortion, and cationic disorder [36, 94, 166]. The NiO_6 and MnO_6 octahedra and La/Sm-O bonds microscopically generate distinct Raman active modes. Generally, NiO_6 and MnO_6 octahedra have two intense modes. In monoclinic structure B_g (~ 540 cm^{-1}) represents anti-stretching (AS) or bending mode, and A_g (~ 670 cm^{-1}) represents stretching (S) or breathing mode [36, 94]. While rhombohedral have A_{1g} (~ 676 cm^{-1}) and E_g (~ 530 cm^{-1}) vibration band known as breathing and bending mode, respectively [167]. The bonds are broader due to the overlapping of nearly similar vibration modes of NiO_6 and MnO_6 octahedra, different structures and the presence of multiple charge valence. The peak intensities and FWHM both are sensitive to Jahn-Teller distortion (due to the presence of Mn^{3+} and Ni^{3+}), oxygen sublattice & vacancies and defect and distortion. Therefore, defining the crystal structure from Raman spectroscopy is difficult. To quantify the antisites disorder variation with Sm proportion, we recorded Raman spectra of $La_{2-x}Sm_xNiMnO_6$ (where $x = 0, 0.1, 0.2$) at 300 and 81 K, respectively in Figure (4.9(a & b)). All samples S_0, S_1, and S_2 have dominated AS and S band around across 540 cm^{-1} and 680 cm^{-1}. It is confirmed that the intensity of these band decreases with the small doping of Sm and with increasing Sm fraction the intensities of the band also increases. Reducing the Sm-doping in $La_{2-x}Sm_xNiMnO_6$ changes into biphasic (monoclinic + rhombohedral) structure into a single monoclinic structure with lower symmetry. Further increased Sm-concentration increases the intensity of bands, indicating increasing cationic ordering, *i.e.*, a reduced degree of antisites disorder. Iliev *et al.* [167], reported the variation of photon frequency and magnetization with the expression: $\Delta\omega \propto M^2(T)$, where M(T) average magnetization at temperature (T).

At low temperatures, peak shifting is directly related to changes in the magnetic state of samples that indicates M_s value get larger as cation ordering increases. The reduction of antisites disorder is due to the small doping of Sm interacting with Ni(Mn) that further enhances the cation ordering. The peak position and FWHM of AS and S peak variation with Sm-concentration at 300 and 81 K are shown in Fig. (4.9(c & d)). The mode frequency (ω) is defined as $\omega \propto \sqrt{(k/m)}$; where m denotes the reduced mass and k is the spring constant. Hence, La substituted with Sm shows higher mass number shifts in the mode of frequency that is consistent with experimental observation, commonly known as *mode*

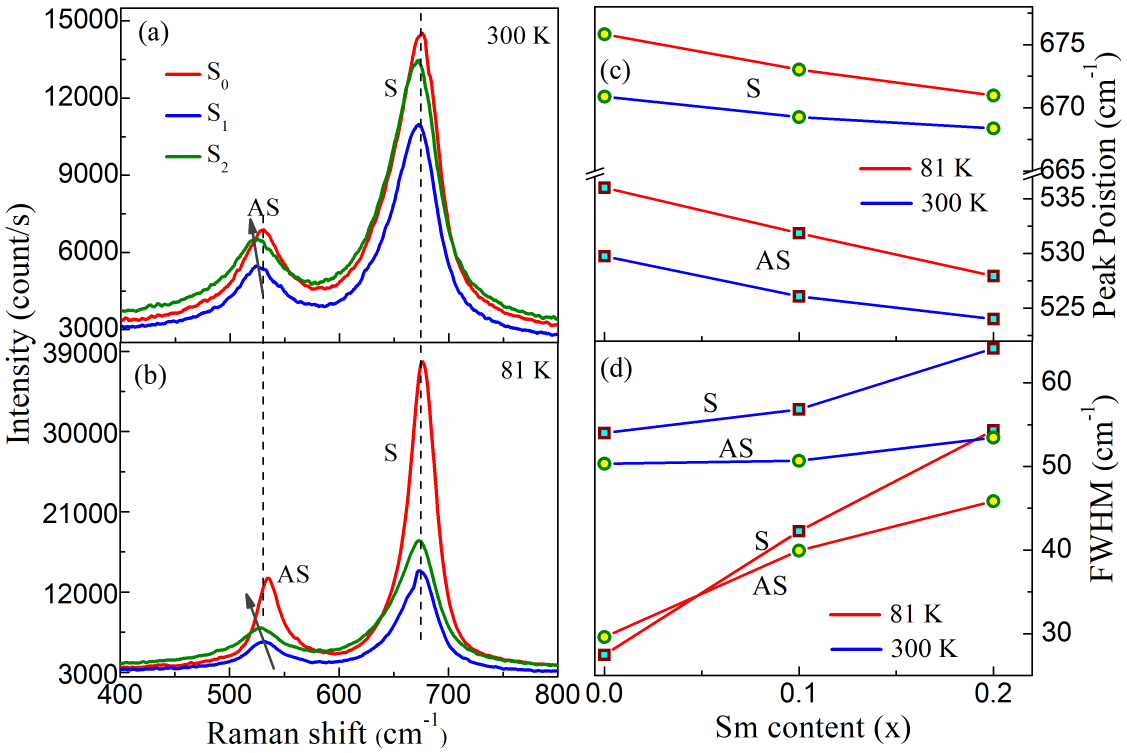

Fig. 4.9 (a) Raman spectra of samples S_0, S_1, and S_2 at 300 K, (b) at 81 K, (c) shifting in the peak position of stroke (S) and antistroke (AS) peaks with Sm-concentration, (d) full width at half maxima (FWHM) shift of S and AS bands as a function of Sm-proportion.

softening. The shifting of the B_g mode is greater than that of the A_g mode, implying that Sm doping affects the bending of $(Ni/Mn)O_6$ octahedra distortion/tilting. It's clear from Fig. (4.9) that with Sm proportion peak position shows a blue shift. The decreases in peak positions with Sm doping due to strain as Sm has lower ionic radii. At low temperatures, atomic vibrations are less causing an increase in electron-phonon coupling which influences the peak intensity and FWHM. Raman spectroscopy of $La_{2-x}Sm_xNiMnO_6$ compounds indicates that Sm doping decreases the degree of antisites disorder.

4.3 Conclusion

In conclusion, Sm-substitution is used to transform the biphasic (monoclinic + rhombohedral) double perovskite structure of LNMO into a single-phase monoclinic system. Sm presence in $La_{2-x}Sm_xNiMnO_6$ improves cation ordering $(Ni/Mn)O_6$ by suppressing the degree of antisite disorder. Experimental finding reveal that Sm-substitution enhances satu-

ration magnetization, and reduces coercive field. Further, a decrease in T_C and enhanced T_{SG} is also reported upon Sm-substitution. The observation of magnetization relaxation, memory, and rejuvenation effect confirms the existence of the spin-glass phase at a lower temperature. Antiphase boundaries in spin-glass phases induce the exchange bias that is tunable with Sm-concentration. The Raman spectra also corroborate that the degree of antisite disorder improved upon Sm-substitution. Our experimental findings confirm that A-site substitution can be stabilized the spin-glass phase in double perovskites.